1

Introduction of the Metastable-Phase Materials

Qi Shao[1] *and Mingwang Shao*[2]

[1] *Soochow University, College of Chemistry, Chemical Engineering and Materials Science, Suzhou, 215123, Jiangsu, China*
[2] *Soochow University, Institute of Functional Nano & Soft Materials (FUNSOM), Jiangsu Key Laboratory for Carbon-Based Functional Materials & Devices, Suzhou, 215123, Jiangsu, China*

1.1 Introduction

From the point of classical thermodynamics, no metastable-phase can exist [1]. Yet, when we look around our world, the number of metastable-phase materials is so huge that it is predominantly larger than that of stable-phase ones. For simple chemical compounds, the ratio of metastable-phases to stablephases is not large. However, the number of metastable compounds becomes dramatically large for complex chemicals, such as organic ones and polymers [2]. For biological materials, nearly 100% phases are metastable ones [3]. Therefore, we can say with certainty: The more complex the materials, the larger the number of metastable-phases.

Such a huge number of metastable-phase materials will certainly bring out interesting and important properties, which may find wide applications in the energy, material, industry, agriculture, biology, environmental, and catalysis-related fields [4]. It should be pointed out that in this book the authors have tried to emphasize on classification, synthetic methodology, characterization, and catalytic performance of different metastable-phase materials.

1.2 What Are Metastable-Phase Materials?

A metastable-phase material is the matter located in a state that corresponds to a local minimum in energy separated by a barrier from the state corresponding to the global minimum. Metastable-phases are in a nonequilibrium state and thus show thermodynamic instability [5]. The energy barrier ensures the metastability and keeps the metastable-phase materials from transformation to stable states, as shown in Figure 1.1.

Metastable-Phase Materials: Synthesis, Characterization, and Catalytic Applications,
First Edition. Edited by Qi Shao, Zhenhui Kang, and Mingwang Shao.

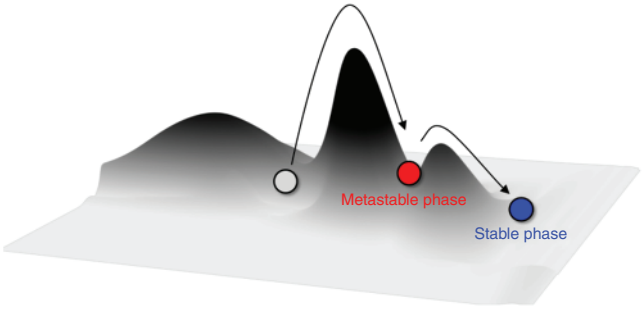

Figure 1.1 The schematic of metastable-phase and stable-phase. The red ball and the blue ball point to metastable-phase and stable-phase, respectively.

Some metastable-phase materials may exist for a long time, such as diamond, which may exist virtually infinitely at room temperature. However, some only exist for a very short time, such as β-Sn, which may exist only for a few days at a temperature of −20 °C and then transform to α-Sn [6].

1.3 The Categories of Metastable-Phase Materials

Considering the large number of metastable-phase materials, several classifications for metastable-phase materials are highly recommended.

From the point of crystallinity, metastable-phases may be classified as crystalline metastable-phases, microcrystalline metastable-phases, quasicrystalline metastable-phases, and amorphous metastable-phases.

Microcrystalline metastable-phase materials, or nanocrystalline metastable-phase materials, have large surface energy, which is favorable to the stability of metastable-phases [7]. These materials have numerous grain boundaries and defects, which bring out larger values of hardness, strength, heat capacity, electrical resistivity, and magnetism [8].

Quasicrystalline metastable-phase materials show lack of transition symmetry [9]. These materials usually have low surface energy, low friction ecoefficiency, but high values of wear resistance, hardness, high-temperature plasticity, thermal resistance, corrosion resistance [10].

Amorphous metastable-phase materials have short-range order and long-range disorder [11]. They have excellent soft magnetic performance and high values of strength and corrosion resistance [12, 13].

This book will focus on the crystalline metastable-phase materials only.

As metastable-phases, together with their corresponding stable-phases, form polymorphs, we classified polymorphs according to the chemical bonds and the coordination environment.

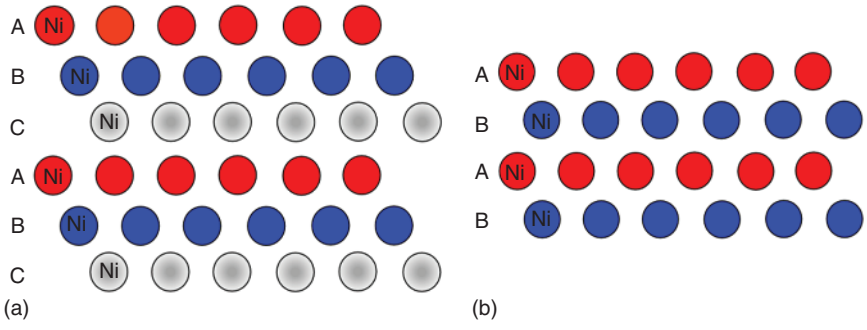

Figure 1.2 The crystal structures of (a) α-Ni and (b) β-Ni.

1.3.1 Different Packing Orders

These polymorphs have the same layers with identical composition, coordination environment, connection mode of coordination. Yet, there are differences in the packing order of these layers.

The typical examples are α-Ni and β-Ni (Figure 1.2), where α-Ni is the stable-phase, while β-Ni is a metastable-phase one. Both of them are coordinated with the number of 12. Each layer of these two materials is composed of the closest packing Ni atoms, with one Ni atom surrounded by six Ni in one layer. Their difference is in the packing order, α-Ni is packed with the order of ABC and β-Ni is AB [14]. The ABC packing endows α-Ni with strong ferromagnetism, while the magnetism of β-Ni is so weak that it can be ignored [15, 16].

The number of this kind of polymorphs is extraordinarily large because only a small amount of energy is needed to alter the packing order. Both SiC and ZnS have hundreds of polymorphs with different packing orders [17, 18].

1.3.2 Different Connecting Modes

These polymorphs have the same coordination polyhedron but different connection modes of these polyhedra. The typical example is TiO_2. Rutile-, anatase-, and brookite-TiO_2 have the same TiO_6 coordination octahedron (Figure 1.3) [19]. Although their connection mode shares edge and corner together, rutile-, anatase-, and brookite-TiO_2 share 2, 4, and 3 edges, respectively, among which rutile-TiO_2 is the most stable material [20].

As the energy to alter connection mode is larger than that for packing order, the number of this kind of polymorphs is less than that of previous ones.

1.3.3 Different Coordination Number

Different coordination number indicates the formation or breaking of chemical bonds, which often involves a large amount of energy [21]. Therefore the number of this kind of polymorphs is small.

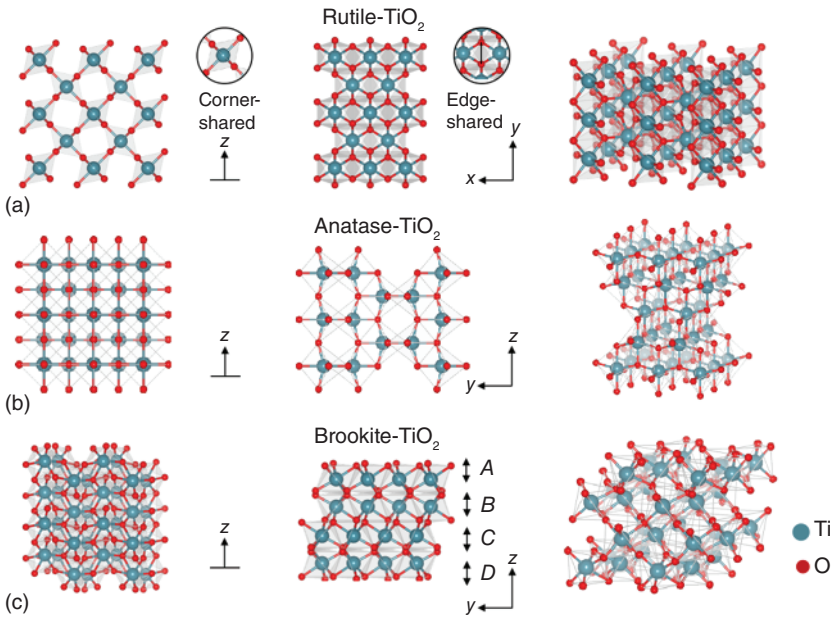

Figure 1.3 The crystal structures of (a) rutile-, (b) anatase-, and (c) brookite-TiO_2.

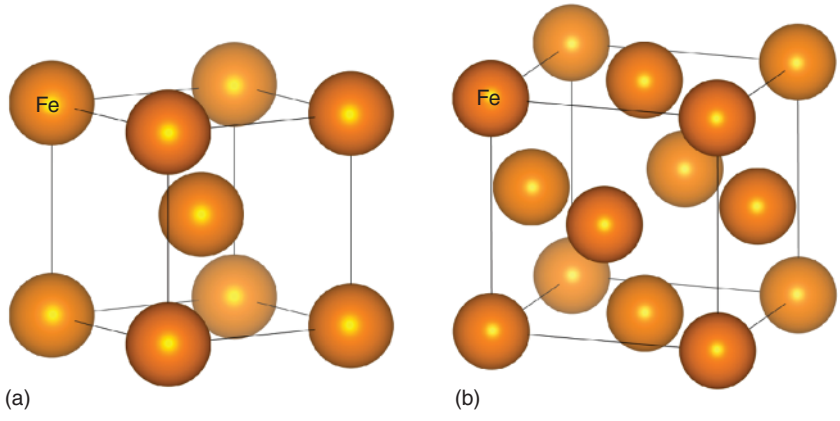

Figure 1.4 The crystal structures of (a) α- and (b) γ-Fe.

The typical example of this kind of polymorphs is iron (Fe). The α- and γ-Fe have body-centered cubic and face-centered cubic phases (Figure 1.4), with the coordination numbers of 8 and 12, respectively [22].

1.3.4 Different Kinds of Chemical Bonds

There are only a few examples for this kind of polymorphs. For example, α- and β-Sn are formed with covalent bonds and metallic bonds, respectively (Figure 1.5) [23]. Another example is carbon, where graphite has a mixture of covalent bonds

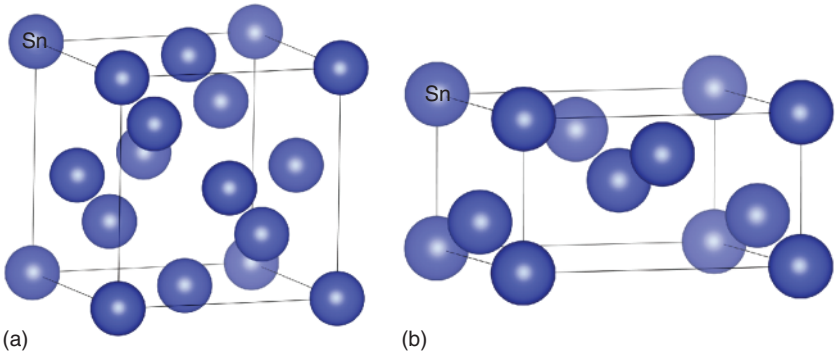

Figure 1.5 The crystal structures of (a) α- and (b) β-Sn.

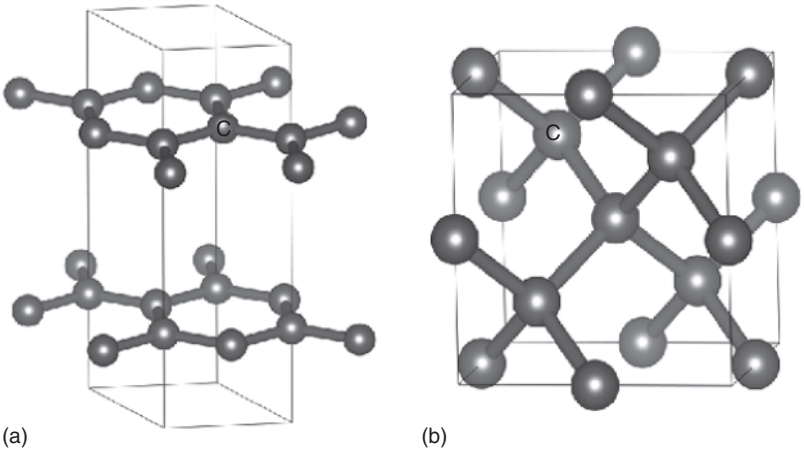

Figure 1.6 The crystal structures of (a) graphite and (b) diamond.

and van der Waals bonds, while diamond is composed of pure covalent bonds (Figure 1.6) [24, 25].

1.3.5 Order and Disorder Polymorphs

Order and disorder polymorphs generally exist in alloys and metallic compounds. At low temperatures, different kinds of atoms were arranged orderly to form crystals with low symmetry; and at high temperature, these atoms occupy the positions disorderly to obtain crystals with high symmetry [26].

For example, FeAl alloy is a simple cube at low temperatures and becomes a body-centered cube at high temperatures (Figure 1.7) [27, 28].

1.3.6 Molecular Thermal-Motion-Related Polymorphs

Temperature also has a significant effect on crystals with ionic groups [29]. As the temperature rises, the thermal vibration of ionic groups becomes so obvious that

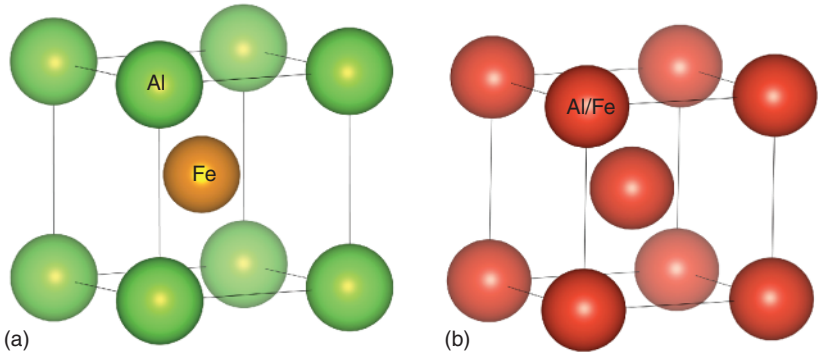

Figure 1.7 The crystal structures of FeAl alloy at (a) low and (b) high temperatures.

these groups may rotate freely showing spherical symmetry, leading to the high symmetry of crystal [30]. For example, NaCN and KCN have low symmetry at low temperatures and form rocksalt structure at high temperatures [31].

Organic compound $C_{29}H_{60}$, whose carbon atoms are connected by the chain-like mode, belongs to the orthorhombic system at low temperatures [32]. As the temperature increases, the molecule rotates around the long axis and has cylindrical symmetry, leading to hexagonal crystal system.

1.3.7 Spin-Related Polymorphs

The polymorphs have the same in X-ray diffraction patterns. Yet, neutron diffraction can discover their differences due to the spin variation.

For example, α-Fe becomes β-Fe when temperature is over 770 °C [33]. Although both of them are body-centered cubic phase, the former one is spin-order and the latter one is spin-disorder. Another example is the superconductor, $YBa_2Cu_3O_{7-\delta}$ when the temperature is below 90 K. It becomes a common conductor with temperature over 90 K [34].

1.4 The Influence on Polymorphs of Materials

1.4.1 Temperature

In this case, as the temperature rises, the coordination number of crystals decreases and crystal symmetry increases [35]. As shown in Table 1.1, metals Ti, Zr, and Tl are in hexagonal closest packing ordering at low temperatures and become body-centered cubic ordering at high temperatures [36–38]. In this process, the coordination number decreases from 12 to 8.

1.4.2 Pressure

When increasing the pressure, the coordination number of crystals will increase and the crystal symmetry will decrease.

Table 1.1 The effect of temperature on polymorphs.

Name	Crystal structure at low *T*	Coordination number at low *T*	Crystal structure at high *T*	Coordination number at high *T*
CsCl	CsCl	8 : 8	NaCl	6 : 6
RbCl	CsCl	8 : 8	NaCl	6 : 6
Ti	HCP	12	BCC	8
Zr	HCP	12	BCC	8
Tl	HCP	12	BCC	8
$CaCO_3$	Aragonite	9	Calcite	6
KNO_3	Aragonite	9	Calcite	6

Table 1.2 The effect of pressure on polymorphs.

Name	Crystal structure at low *P*	Coordination number at low *p*	Crystal structure at high *P*	Coordination number at high *P*
RbCl	NaCl	6 : 6	CsCl	8 : 8
RbBr	NaCl	6 : 6	CsCl	8 : 8
RbI	NaCl	6 : 6	CsCl	8 : 8
Cs	BCC	8	FCC	12
Fe	BCC	8	FCC	12
GeO_2	Quartz	4 : 2	Rutile	6 : 3

As shown in Table 1.2, metals Cs and Fe are body-centered cubic phase at ambient pressure and become face-centered cubic phase with increasing pressure. Their coordination numbers also increase from 8 to 12 [39, 40].

1.4.3 The Stability in Nano-size Metastable-Phase Catalysts

The metastable-phase catalysts may achieve dual improvement in catalytic activity and stability. Let us explain our assertion.

The sizes of catalysts are often in nano-scale to obtain maximum utilization of catalyst atoms. And metastable-phase materials may have high catalytic activity due to their high free energy. It is generally believed that the stability of metastable-phases is the biggest challenge in the development of metastable-phase catalysts. Yet, in fact, it is not necessarily like that.

Although the stability of the metastable-phase in bulk is not as good as its corresponding stable-phase, at the nanoscale, the stability of the metastable-phase may be higher than that of the stable-phase. For example, anatase titanium dioxide with a size less than 10 nm is higher than rutile of the same size.

In addition, dimension is also a consideration, as two-dimensional materials only have van der Waals bonds between layers, resulting in small surface energy. Therefore, two-dimensional materials are often more stable than their corresponding three-dimensional stable-phases. Iridium dioxide in the 1T phase is more stable than iridium dioxide in rutile.

In short, the low dimension and/or small size endow metastable-phase catalysts with higher catalytic activity and stability than their corresponding stable ones.

1.5 The Wide Applications of Metastable-Phase Materials

Metastable-phase materials with novel properties are essential to solving enormous future challenges, such as energy crisis, food safety, resource depletion, and environmental pollution [41].

These applications include catalysts [42], photocatalysts [43], electrocatalysts [44], semiconductors [45], magnets [46], ion conductors [47], superconductors [48], thermoelectrics [49], photoluminescent materials [50], and sensors [51].

1.6 The Criterion for Stable-Phase and Metastable-Phase Materials

The following discussion is about the criterion for stable-phase metals and metastable-phase metals.

There is always an inequality (1.1), on the basis of the definition of metastable-phases.

$$\Delta G^0_{f,\text{stable-phase}} < \Delta G^0_{f,\text{metastable-phase}} \tag{1.1}$$

Or

$$\Delta H^0_{f,\text{stable-phase}} - T_{298\ \text{K}}\Delta S^0_{f,\text{stable-phase}} < \Delta H^0_{f,\text{metastable-phase}} - T_{298\ \text{K}}\Delta S^0_{f,\text{metastable-phase}}$$

As both the stable-phase and metastable-phase are solid, the difference between $\Delta S^0_{f,\text{stable-phase}}$ and $\Delta S^0_{f,\text{metastable-phase}}$ is very small.

Therefore, the inequality is often correct.

$$\Delta H^0_{f,\text{stable-phase}} < \Delta H^0_{f,\text{metastable-phase}}$$

On the other hand, bond energy, or bond disruption energy, is defined as the standard enthalpy change of the following fission: $\text{R} - \text{X} \rightarrow \text{R} + \text{X}$, denoted by $D^0(\text{R} - \text{X})$. And the enthalpy of formation may be approximated as the sum of bond energies.

$$\Delta H^0_f = -\sum_{\text{all}} D^0_i$$

So, we may obtain:

$$\sum_{\text{all}} D^0_{i,\text{stable-phase}} > \sum_{\text{all}} D^0_{i,\text{metastable-phase}}$$

For a given chemical bond, its bond energy is inversely proportional to bond length [52, 53].

Huggins gave an equation for bond energy and bond length,

$$D = \exp[a(r_0 - r)],$$

where D is bond energy, r bond length, and a and r_0 are constant for a given bond.

$$\sum_{\text{all}} \exp(-ar_i)_{\text{stable-phase}} > \sum_{\text{all}} \exp(-ar_i)_{\text{metastable-phase}}$$

For both stable-phase and metastable-phase, if the nature of their chemical bonds is the same, the following inequality is present, as a rough approximation,

$$\sum_{\text{all}} ar_{i\text{stable-phase}} < \sum_{\text{all}} ar_{i\text{metastable-phase}}.$$

Here, a is a parameter related with the crystal structure. After a broad investigation, $a \propto \left(\frac{V}{Z}\right)^{\frac{1}{3}}$. V is the volume of crystal cells and Z is the number of chemical formulas in a crystal cell.

The above equation may be re-written as:

$$\left(\frac{V}{Z}\right)^{\frac{1}{3}}_{\text{stable-phase}} \sum_{\text{all}} r_{i\text{stable-phase}} < \left(\frac{V}{Z}\right)^{\frac{1}{3}}_{\text{metastable-phase}} \sum_{\text{all}} r_{i\text{metastable-phase}} \tag{1.2}$$

Furthermore, if the coordination numbers of stable-phase and metastable-phase are the same, we may obtain

$$\left(\frac{V}{Z}\right)^{\frac{1}{3}}_{\text{stable-phase}} r_{\text{average,stable-phase}} < \left(\frac{V}{Z}\right)^{\frac{1}{3}}_{\text{metastable-phase}} r_{\text{average,metastable-phase}}. \tag{1.3}$$

For example, TiO_2 has many crystal structures and the main important ones are rutile, anatase, and brookite. All these three have TiO_6 coordination octahedron with various connected modes. Therefore, we may use Eq. (1.3) to determine which one is the stable-phase. Based on the calculation (Table 1.3), rutile is the stable-phase while others are metastable-phases, because the value of $\left(\frac{V}{Z}\right)^{\frac{1}{3}} r_{\text{average}}$ for rutile is the smallest.

Table 1.3 The criterion to determine stable-phase and metastable-phase for rutile, anatase, and brookite TiO_2.

Material	Unit-cell dimension	$\left(\frac{V}{Z}\right)^{\frac{1}{3}}$	r_{average}	$\left(\frac{V}{Z}\right)^{\frac{1}{3}} r_{\text{average}}$
Rutile TiO_2	$a = b = 4.60$ Å, $c = 2.96$ Å; $\alpha = \beta = \gamma = 90.00°$	3.148	1.961	6.172
Anatase TiO_2	$a = b = 3.78$ Å, $c = 9.62$ Å; $\alpha = \beta = \gamma = 90.00°$	3.240	1.544°	6.332
Brookite TiO_2	$a = 5.15$ Å, $b = 5.46$ Å, $c = 9.19$ Å; $\alpha = \beta = \gamma = 90.00°$	3.182	1.963	6.244

References

1 Alert, R., Tierno, P., and Casademunt, J. (2016). Formation of metastable phases by spinodal decomposition. *Nature Communications* 7: 13067.

2 Sasaki, S., Caldes, M.T., Guillot-Deudon, C. et al. (2021). Design of metastable oxychalcogenide phases by topochemical (de)intercalation of sulfur in $La_2O_2S_2$. *Nature Communications* 12 (1): 3605.

3 Kocevski, V., Valdez, J.A., Derby, B.K. et al. (2023). Predicting and accessing metastable phases. *Materials Advances* 4 (4): 1101–1112.

4 Wang, C.X. and Yang, G.W. (2005). Thermodynamics of metastable phase nucleation at the nanoscale. *Materials Science & Engineering R – Reports* 49 (6): 157–202.

5 Bechhoefer, J., Löwen, H., and Tuckerman, L.S. (1991). Dynamical mechanism for the formation of metastable phases. *Physical Review Letters* 67 (10): 1266–1269.

6 Di Maio, D. and Hunt, C. (2009). Time-lapse photography of the β-Sn/α-Sn allotropic transformation. *Journal of Materials Science: Materials in Electronics* 20 (4): 386–391.

7 Li, H.B., Zanella, M., Genovese, A. et al. (2011). Sequential cation exchange in nanocrystals: preservation of crystal phase and formation of metastable phases. *Nano Letters* 11 (11): 4964–4970.

8 Ayyub, P., Multani, M., Barma, M. et al. (1988). Size-induced structural phase transitions and hyperfine properties of microcrystalline Fe_2O_3. *Journal of Physics C – Solid State Physics* 21 (11): 2229–2245.

9 Urgel, J.I., Ecija, D., Lyu, G.Q. et al. (2016). Quasicrystallinity expressed in two-dimensional coordination networks. *Nature Chemistry* 8 (7): 657–662.

10 Yoshida, T., Itoh, K., Tamura, R., and Takeuchi, S. (2000). Plastic deformation and hardness in Mg-Zn-(Y, Ho) icosahedral quasicrystals. *Materials Science and Engineering A – Structural Materials Properties* 294: 786–789.

11 Shi, L., Zhang, Y.F., Dong, B.Q. et al. (2013). Amorphous photonic crystals with only short-range order. *Advanced Materials* 25 (37): 5314–5320.

12 Patil, U., Hong, S.H., and Suryanarayana, C. (2005). An unusual phase transformation during mechanical alloying of an Fe-based bulk metallic glass composition. *Journal of Alloys and Compounds* 389 (1-2): 121–126.

13 Suryanarayana, C. (2019). Mechanical alloying: a novel technique to synthesize advanced materials. *Research* 2019: 17.

14 Chandran, M. and Sondhi, S.K. (2011). First-principle calculation of stacking fault energies in Ni and Ni-Co alloy. *Journal of Applied Physics* 109 (10): 103525.

15 Hossain, M.D., Mayanovic, R.A., Dey, S. et al. (2018). Room-temperature ferromagnetism in Ni (II)-chromia based core–shell nanoparticles: experiment and first principles calculations. *Physical Chemistry Chemical Physics* 20 (15): 10396–10406.

16 Davar, F., Fereshteh, Z., and Salavati-Niasari, M. (2009). Nanoparticles Ni and NiO: synthesis, characterization and magnetic properties. *Journal of Alloys and Compounds* 476 (1-2): 797–801.

17 Fang, X.S., Zhai, T.Y., Gautam, U.K. et al. (2011). ZnS nanostructures: from synthesis to applications. *Progress in Materials Science* 56 (2): 175–287.

18 Matsunami, H. and Kimoto, T. (1997). Step-controlled epitaxial growth of SiC: High quality homoepitaxy. *Materials Science & Engineering R – Reports* 20 (3): 125–166.

19 Kaplan, R., Erjavec, B., Dražić, G. et al. (2016). Simple synthesis of anatase/rutile/brookite TiO_2 nanocomposite with superior mineralization potential for photocatalytic degradation of water pollutants. *Applied Catalysis B – Environmental* 181: 465–474.

20 Gao, C.M., Wei, T., Zhang, Y.Y. et al. (2019). A photoresponsive rutile TiO_2 heterojunction with enhanced electron–hole separation for high-performance hydrogen evolution. *Advanced Materials* 31 (8): 1806596.

21 Wang, L.L., Zhu, C.W., Xu, M.Q. et al. (2021). Boosting activity and stability of metal single-atom catalysts via regulation of coordination number and local composition. *Journal of the American Chemical Society* 143 (45): 18854–18858.

22 He, Y., Li, Y.J., Chen, C.F., and Yu, H.B. (2017). Diffusion coefficient of hydrogen interstitial atom in α-Fe, γ-Fe and ε-Fe crystals by first-principle calculations. *International Journal of Hydrogen Energy* 42 (44): 27438–27445.

23 Haq, A.U., Askari, S., McLister, A. et al. (2019). Size-dependent stability of ultra-small α-/β-phase tin nanocrystals synthesized by microplasma. *Nature Communications* 10 (1): 817.

24 Ooi, N., Rairkar, A., and Adams, J.B. (2006). Density functional study of graphite bulk and surface properties. *Carbon* 44 (2): 231–242.

25 Erdemir, A. and Martin, J.M. (2018). Superior wear resistance of diamond and DLC coatings. *Current Opinion in Solid State & Materials Science* 22 (6): 243–254.

26 Kim, K., Arora, A., Lewis, R.M. III, et al. (2018). Origins of low-symmetry phases in asymmetric diblock copolymer melts. *Proceedings of the National Academy of Sciences of the United States of America* 115 (5): 847–854.

27 Kupka, M. (2006). High temperature strengthening of the FeAl intermetallic phase-based alloy. *Intermetallics* 14 (2): 149–155.

28 Baker, I. and Munroe, P.R. (1997). Mechanical properties of FeAl. *International Materials Reviews* 42 (5): 181–205.

29 Liu, Q., Liao, Z.R., and Axinte, D. (2020). Temperature effect on the material removal mechanism of soft-brittle crystals at nano/micron scale. *International Journal of Machine Tools & Manufacture* 159: 103620.

30 Chang, C., Wu, M.H., He, D.S. et al. (2018). 3D charge and 2D phonon transports leading to high out-of-plane ZT in n-type SnSe crystals. *Science* 360 (6390): 778–783.

31 Ushkov, A.V. and Grushin, V.V. (2011). Rational catalysis design on the basis of mechanistic understanding: highly efficient Pd-catalyzed cyanation of aryl bromides with NaCN in recyclable solvents. *Journal of the American Chemical Society* 133 (28): 10999–11005.

32 Mare, E.R., O'Neill, H.S.C., Berry, A.J. et al. (2021). Coordination change of Ge^{4+} and Ga^{3+} in silicate melt with pressure. *Geochimica Et Cosmochimica Acta* 303: 184–204.

33 Vershinina, T.N., Bobrikov, I.A., Sumnikov, S.V. et al. (2021). Crystal structure and phase composition evolution during heat treatment of Fe-45Ga alloy. *Intermetallics* 131: 107110.

34 Soderholm, L., Zhang, K., Hinks, D.G. et al. (1987). Incorporation of Pr in $YBa_2Cu_3O_7$-δ: electronic effects on superconductivity. *Nature* 328 (6131): 604–605.

35 Mary, T.A., Evans, J.S.O., Vogt, T., and Sleight, A.W. (1996). Negative thermal expansion from 0.3 to 1050 Kelvin in ZrW_2O_8. *Science* 272 (5258): 90–92.

36 Assi, H., Mouchaham, G., Steunou, N. et al. (2017). Titanium coordination compounds: from discrete metal complexes to metal-organic frameworks. *Chemical Society Reviews* 46 (11): 3431–3452.

37 Lv, D.F., Chen, J.Y., Chen, Y.W. et al. (2019). Moisture stability of ethane-selective Ni (II), Fe (III), Zr (IV)-based metal-organic frameworks. *AIChE Journal* 65 (8): e16616.

38 Karasev, M.O., Karaseva, I.N., and Pushkin, D.V. (2021). MC_n (M= Ga, In, Tl) coordination polyhedra in crystal structures. *Russian Journal of Inorganic Chemistry* 66: 1669–1681.

39 Xie, Y., Ma, Y.M., Cui, T. et al. (2008). Origin of bcc to fcc phase transition under pressure in alkali metals. *New Journal of Physics* 10 (6): 063022.

40 Matsui, M. and Anderson, O.L. (1997). The case for a body-centered cubic phase (α′) for iron at inner core conditions. *Physics of the Earth and Planetary Interiors* 103 (1-2): 55–62.

41 Therrien, F., Jones, E.B., and Stevanović, V. (2021). Metastable materials discovery in the age of large-scale computation. *Applied Physics Reviews* 8 (3): 031310.

42 Zhang, Z., Zandkarimi, B., and Alexandrova, A.N. (2020). Ensembles of metastable states govern heterogeneous catalysis on dynamic interfaces. *Accounts of Chemical Research* 53 (2): 447–458.

43 Zhang, Y.Z., Zhou, W., Tang, Y. et al. (2022). Unravelling unsaturated edge S in amorphous NiS_x for boosting photocatalytic H_2 evolution of metastable phase CdS confined inside hydrophilic beads. *Applied Catalysis B – Environmental* 305: 121055.

44 Wen, W.D., Yan, P., Sun, W.P. et al. (2023). Metastable phase Cu with optimized local electronic state for efficient electrocatalytic production of ammonia from nitrate. *Advanced Functional Materials* 33 (6): 2212236.

45 Caskey, C.M., Richards, R.M., Ginley, D.S., and Zakutayev, A. (2014). Thin film synthesis and properties of copper nitride, a metastable semiconductor. *Materials Horizons* 1 (4): 424–430.

46 Balasubramanian, B., Zhao, X., Valloppilly, S.R. et al. (2018). Magnetism of new metastable cobalt-nitride compounds. *Nanoscale* 10 (27): 13011–13021.

47 Zhou, L.J., Xu, J.G., Allix, M., and Kuang, X.J. (2020). Development of melilite-type oxide ion conductors. *Chemical Record* 20 (10): 1117–1128.

48 Budden, M., Gebert, T., Buzzi, M. et al. (2007). Evidence for metastable photo-induced superconductivity in K_3C_{60}. *Nature Physics* 17 (5): 611–618.

49 Ikeda, T., Collins, L.A., Ravi, V.A. et al. (2007). Self-assembled nanometer lamellae of thermoelectric PbTe and Sb_2Te_3 with epitaxy-like interfaces. *Chemistry of Materials* 19 (4): 763–767.

50 Cao, H.Q., Qiu, X.Q., Luo, B. et al. (2004). Synthesis and room-temperature ultraviolet photoluminescence properties of zirconia nanowires. *Advanced Functional Materials* 14 (3): 243–246.

51 Righettoni, M., Tricoli, A., and Pratsinis, S.E. (2010). Thermally stable, silica-doped ε-WO_3 for sensing of acetone in the human breath. *Chemistry of Materials* 22 (10): 3152–3157.

52 Clark, C.H.D. (1939). Interrelation of dissociation energy, internuclear distance and bond order for carbon-carbon linkages. *Nature* 143 (3628): 800–801.

53 Huggins, M.L. (1953). Atomic radii. IV. Dependence of interatomic distance on bond energy. *Journal of the American Chemical Society* 75: 4126–4133.